inter.noise
HAMBURG 2016

On the sunflower spiral: acoustical holography results

Christof Puhle[1], Sébastien Barré[1] and Sean Hollands[2]
[1]Society for the Advancement of Applied Computer Science, GFaI e.V., Germany
[2]Polytec, Inc., USA

ABSTRACT

The sunflower spiral is an element of a family of well understood patterns which appear in many biological settings, e.g. in the formation of leaves or seeds in a flower. We study a multi-purpose phased array whose microphones are arranged in this particular form. More precisely, we investigate the influence of this arrangement on both beamforming and holography results. To render (near-field) acoustical holography possible given the shape of the array, we choose both, a Helmholtz equation least-squares and statistically optimized NAH approach. Our considerations include the analysis of experimental data of a vibrating plate: the results of both holography methods are compared against a laser vibrometer measurement.

Keywords: Phased array, acoustical holography, HELS, SONAH

CONTENTS

1. THE SUNFLOWER SPIRAL

The positions of the individual microphones in an array together with the used evaluation method determines the information gathered by it. In [1], a general argument shows that for any fixed number of microphones, non-redundant arrangements produce the best beamforming results. While easy to realize in practice, classical arrangements like the equilateral grid or circular arrangements do not fall into this category. As the most prominent class of non-redundant arrangements, spirals were shown to have favorable beamforming properties (see [2–5]). On the contrary, evenly distributed microphones are known to form the best arrays for acoustical holography (cf. [6]).

In [5], Sarradj studied a three-parameter family of microphone arrangements which generalizes Vogel's spiral (see [7]). In polar coordinates, the microphone positions

$$(r_1, \phi_1), \ldots, (r_N, \phi_N) \tag{1}$$

are parametrized by $R, V, H \in \mathbb{R}$, $R, V > 0$,

$$r_n = \sqrt{\sum_{m=1}^{n} \frac{2\int_0^R f_H(r) r dr}{N f_H(r_m)}},$$

$$\phi_n = 2\pi n \frac{\sqrt{V}+1}{2}. \tag{2}$$

Here, the radial weighting function $f_H : [0, R] \to \mathbb{R}$ is defined via

$$f_H(r) = \left(I_0 \left(\pi H \sqrt{1 - \left(\frac{r}{R}\right)^2} \right) \right)^{\operatorname{sgn}(H)}, \tag{3}$$

and I_0 denotes the modified Bessel function of the first kind of order zero.

From the viewpoint of acoustical holography, the case of uniform or no radial weighting ($H = 0$) is certainly the best choice. In this case, system (2) reduces to

$$\begin{aligned} r_n &= R\sqrt{\frac{n}{N}}, \\ \phi_n &= 2\pi n \frac{\sqrt{V}+1}{2}. \end{aligned} \tag{4}$$

In addition, Ridley showed that among these arrangements, the so-called sunflower spiral, i.e. $V = 5$, has the most efficient packing pattern. More precisely, the infimum of distances between microphones is maximized in this case (see [8]). From the viewpoint of beamforming, the case $V = 5$ has Pareto-optimal properties in terms of beam width and maximum side lobe level of the corresponding point spread function (see [5]).

The multi-purpose phased array we are considering consists of two sunflower spirals with

$$R = \frac{\sqrt{6}}{7}, \frac{\sqrt{6}}{14} \tag{5}$$

and one central arrangement around the optical cameras. All 120 microphone positions are visualized in Figure 1. Moreover, we plotted the density function of all microphone distances there.

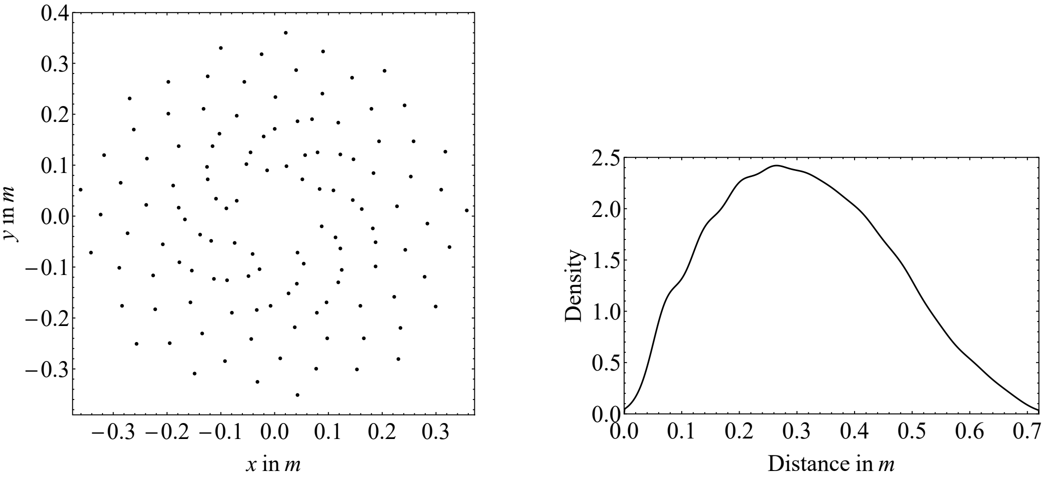

Figure 1. Microphone positions (left) and density function of microphone distances (right)

2. ACOUSTICAL HOLOGRAPHY

In classical near-field acoustical holography (NAH), the sound field of interest is propagated from the measurement plane to the source plane involving a spatial FFT of the measured data. In practice, there are several shortcomings in this method. First of all, the necessity of a spatial Fourier transform limits the geometry of the microphone array in a way that is unacceptable for other methods like beamforming. Moreover, the corresponding spatial window requires the measurement area to be significantly larger than the source. The two acoustical holography methods we are going to introduce in this section overcome these problems. The statistically optimized NAH (SONAH) performs the plane-to-plane transformation in the spatial domain avoiding a spatial FFT (see [9]), and the Helmholtz equation least squares (HELS) method uses an expansion of some basis functions to reconstruct the acoustic pressure in the source plane (see [10]).

2.1 SONAH

Let $p : \mathbb{R}^3 \to \overline{\mathbb{C}}$ be a function that represents the complex amplitude of a time-harmonic sound pressure field of angular frequency ω generated in the half space $z \leq -d$, $d > 0$, the open half space

$$D = \left\{(x, y, z) \in \mathbb{R}^3 \,:\, z > -d\right\} \tag{6}$$

is supposed to be source free. Our sign convention for a time-harmonic function is $t \mapsto \exp(i\omega t)$. For example,

$$p(x, y, z) = \frac{\exp\left(-ik\sqrt{x^2 + y^2 + (z + d)^2}\right)}{\sqrt{x^2 + y^2 + (z + d)^2}}, \quad k = \frac{\omega}{c} \tag{7}$$

represents an outgoing spherical wave with source $(0, 0, -d)$ and speed of propagation c. Weyl showed (see [11]) that this spherical wave satisfies

$$p(x, y, z) = \frac{1}{(2\pi)^2} \int_{\mathbb{R}^2} P\left(k_x, k_y\right) \Psi\left(k_x, k_y, x, y, z\right) d\lambda\left(k_x, k_y\right), \tag{8}$$

where

$$\Psi\left(k_x, k_y, x, y, z\right) = \exp\left(-i\left(k_x x + k_y y + k_z\left(k_x, k_y\right)(z + d)\right)\right), \tag{9}$$

$$P\left(k_x, k_y\right) = \frac{2\pi}{ik_z(k_x, k_y)}, \quad k_z(k_x, k_y) = \begin{cases} \sqrt{k^2 - k_x^2 - k_y^2} & \text{if } k^2 \geq k_x^2 + k_y^2 \\ -i\sqrt{k_x^2 + k_y^2 - k^2} & \text{if } k^2 < k_x^2 + k_y^2 \end{cases}, \tag{10}$$

λ denotes the Lebesgue measure. Written in this form, this fact has an interesting interpretation. The spherical wave p can be understood as a superposition of infinitely many plane waves ($k^2 \geq k_x^2 + k_y^2$) and evanescent waves ($k^2 < k_x^2 + k_y^2$) each caused by a vibration of the so-called source plane

$$S = \left\{(x, y, z) \in \mathbb{R}^3 \,:\, z = -d\right\} \tag{11}$$

with structural wave numbers equal to k_x and k_y. Henceforth, we will restrict our considerations to functions p such that there exists a λ-integrable function $P : \mathbb{R}^2 \to \mathbb{C}$ that satisfies equation (8), i.e. we restrict ourselves to sound pressure fields caused by vibrations of the source plane.

The SONAH method (see [9]) aims at the reconstruction of p at a position $r = (x, y, z) \in S$ in the source plane using a measurement of p at mutually distinct positions $r_1, \ldots, r_N \in D$ in the source-free region. One of the fundamental assumptions of SONAH is that $p(r)$ is approximated by a linear combination of the measured pressures $p(r_1), \ldots, p(r_N)$, i.e.

$$p(r) \approx p_{\text{app}}(r) = \sum_{n=1}^{N} \alpha(r)_n p(r_n), \quad \alpha(r)_1, \ldots, \alpha(r)_N \in \mathbb{C}. \tag{12}$$

Interestingly enough, the set of possible solutions $\alpha(r)_1, \ldots, \alpha(r)_N$ includes the coefficients of frequency domain beamforming. We are going to revisit this fact later in this section.

Since p can be represented as a superposition of functions $\Psi_{k_x,k_y} : \mathbb{R}^3 \to \mathbb{C}$,

$$\Psi_{k_x,k_y}\left(r\right) = \Psi\left(k_x, k_y, x, y, z\right), \tag{13}$$

the SONAH method requires them to be reconstructed through (12) as well. Restricting the consideration to a finite subset of structural wave numbers $(k_x, k_y) \in \mathbb{R}^2$, this requirement leads to a least squares problem for $\alpha(r)_1, \ldots, \alpha(r)_N$. Motivated by certain limits of its (regularized) solution, the SONAH method depicts

$$\alpha(r) = (M + \delta \cdot \mathrm{Id})^{-1} \gamma(r), \tag{14}$$

where

$$M_{nn'} = \left\langle \Psi_{r_n}\,,\, \Psi_{r_{n'}} \right\rangle, \quad \gamma(r)_n = \left\langle \Psi_{r_n}\,,\, \Psi_r \right\rangle, \tag{15}$$

$$\left\langle \Psi_{r_1}\,,\, \Psi_{r_2} \right\rangle = \frac{1}{\pi k^2} \int_{\mathbb{R}^2} \Psi_{r_1}^* \Psi_{r_2} d\lambda, \tag{16}$$

and $\Psi_r : \mathbb{R}^2 \to \mathbb{C}$ is defined via

$$\Psi_r\left(k_x, k_y\right) = \Psi\left(k_x, k_y, x, y, z\right). \tag{17}$$

The parameter δ is given by

$$\delta = \left(1 + \frac{1}{2\left(kd\right)^2}\right) \cdot 10^{-\frac{\sigma}{10}} \tag{18}$$

with σ being the effective signal-to-noise ratio of the measurement in dB.

Let us simplify the scalar products (16) by introducing polar coordinates,

$$\begin{aligned} \left\langle \Psi_{r_1}\,,\, \Psi_{r_2} \right\rangle &= \frac{1}{\pi k^2} \int_0^\infty \int_{-\pi}^{\pi} \exp\left(-i\kappa \Delta_{r_1,r_2} \sin\left(\varphi\right)\right) \\ &\qquad\qquad \cdot \exp\left(ik_z^* z_1 - ik_z z_2\right) \exp\left(i\left(k_z^* - k_z\right) d\right) \kappa d\varphi d\kappa \\ &= \frac{2}{k^2} \int_0^\infty J_0\left(\kappa \Delta_{r_1,r_2}\right) \exp\left(ik_z^* z_1 - ik_z z_2\right) \exp\left(i\left(k_z^* - k_z\right) d\right) \kappa d\kappa. \end{aligned} \tag{19}$$

Here, J_0 denotes the Bessel function of the first kind of order zero and

$$\Delta_{r_1,r_2} = \sqrt{\left(x_1 - x_2\right)^2 + \left(y_1 - y_2\right)^2}. \tag{20}$$

We then split the remaining integral in two parts,

$$\begin{aligned} \left\langle \Psi_{r_1}\,,\, \Psi_{r_2} \right\rangle &= \frac{2}{k^2} \int_0^k J_0\left(\kappa \Delta_{r_1,r_2}\right) \exp\left(i\sqrt{k^2 - \kappa^2}\left(z_1 - z_2\right)\right) \kappa d\kappa \\ &\quad + \frac{2}{k^2} \int_k^\infty J_0\left(\kappa \Delta_{r_1,r_2}\right) \exp\left(-\sqrt{\kappa^2 - k^2}\left(z_1 + z_2 + 2d\right)\right) \kappa d\kappa. \end{aligned} \tag{21}$$

Consequently, the right-hand side of (14) can be computed with the aid of one-dimensional numerical integration.

We now investigate the matrix M and the vector $\gamma(r)$ in case the measurement positions $r_1, \ldots, r_N$ fall into the x-y-plane. Using equation (21), we have

$$M_{nn'} = \frac{2}{k^2} \int_0^k J_0\left(\kappa \Delta_{r_n,r_{n'}}\right) \kappa d\kappa + \frac{2}{k^2} \int_k^\infty J_0\left(\kappa \Delta_{r_n,r_{n'}}\right) \exp\left(-2d\sqrt{\kappa^2 - k^2}\right) \kappa d\kappa. \tag{22}$$

For $n = n'$, this simplifies to

$$\begin{aligned} M_{nn} &= \frac{2}{k^2} \int_0^k \kappa d\kappa + \frac{2}{k^2} \int_k^\infty \exp\left(-2d\sqrt{\kappa^2 - k^2}\right) \kappa d\kappa \\ &= 1 + \frac{2}{k^2} \int_0^\infty \exp\left(-2d\varrho\right) \varrho d\varrho \\ &= 1 + \frac{1}{2(kd)^2}. \end{aligned} \tag{23}$$

Therefore, in the limit of high frequencies, the diagonal elements of M approach 1,

$$\lim_{k\to\infty} M_{nn} = 1. \tag{24}$$

In case $n \neq n'$, we have $\Delta_{r_1,r_2} \neq 0$, and therefore

$$M_{nn'} = 2\frac{J_1\left(k\Delta_{r_n,r_{n'}}\right)}{k\Delta_{r_n,r_{n'}}} + \frac{2}{k^2}\int_k^\infty J_0\left(\kappa\Delta_{r_n,r_{n'}}\right)\exp\left(-2d\sqrt{\kappa^2-k^2}\right)\kappa d\kappa. \tag{25}$$

Let us compute an upper bound for $|M_{nn'}|$:

$$\begin{aligned}
|M_{nn'}| &\leq 2\left|\frac{J_1\left(k\Delta_{r_n,r_{n'}}\right)}{k\Delta_{r_n,r_{n'}}}\right| + \frac{2}{k^2}\left|\int_k^\infty J_0\left(\kappa\Delta_{r_n,r_{n'}}\right)\exp\left(-2d\sqrt{\kappa^2-k^2}\right)\kappa d\kappa\right| \\
&\leq 2\frac{1}{k\Delta_{r_n,r_{n'}}} + \frac{2}{k^2}\int_k^\infty \left|J_0\left(\kappa\Delta_{r_n,r_{n'}}\right)\right|\exp\left(-2d\sqrt{\kappa^2-k^2}\right)\kappa d\kappa \\
&\leq 2\frac{1}{k\Delta_{r_n,r_{n'}}} + \frac{2}{k^2}\int_k^\infty \exp\left(-2d\sqrt{\kappa^2-k^2}\right)\kappa d\kappa \\
&= 2\frac{1}{k\Delta_{r_n,r_{n'}}} + \frac{1}{2(kd)^2}.
\end{aligned} \tag{26}$$

Consequently, M approaches the identity matrix in the limit of high frequencies,

$$\lim_{k\to\infty} M = \mathrm{Id}. \tag{27}$$

The treatise of $\gamma(r)$ is quite similar,

$$\begin{aligned}
\gamma(r)_n = &\frac{2}{k^2}\int_0^k J_0\left(\kappa\Delta_{r_n,r}\right)\exp\left(id\sqrt{k^2-\kappa^2}\right)\kappa d\kappa \\
&+ \frac{2}{k^2}\int_k^\infty J_0\left(\kappa\Delta_{r_n,r}\right)\exp\left(-d\sqrt{\kappa^2-k^2}\right)\kappa d\kappa.
\end{aligned} \tag{28}$$

We begin our discussion with the case $\Delta_{r_n,r} = 0$, that means the reconstruction point is the projection of the n-th measurement position onto the source plane. Here,

$$\begin{aligned}
\gamma(r)_n &= \frac{2}{k^2}\int_0^k \exp\left(id\sqrt{k^2-\kappa^2}\right)\kappa d\kappa + \frac{2}{k^2}\int_k^\infty \exp\left(-d\sqrt{\kappa^2-k^2}\right)\kappa d\kappa \\
&= \frac{2}{k^2}\int_0^k \exp\left(id\varrho\right)\varrho d\varrho + \frac{2}{(kd)^2} \\
&= \frac{2\left(1-ikd\right)}{(kd)^2}\exp\left(ikd\right).
\end{aligned} \tag{29}$$

If the reconstruction point is not the projection of the n-th measurement position, then $\Delta_{r_n,r} \neq 0$ and

$$\begin{aligned}
|\gamma(r)_n| &\leq \frac{2}{k^2}\int_0^k \sqrt{\frac{2}{\pi\kappa\Delta_{r_n,r}}}\kappa d\kappa + \frac{2}{k^2}\int_k^\infty \exp\left(-d\sqrt{\kappa^2-k^2}\right)\kappa d\kappa \\
&= \frac{4}{3}\sqrt{\frac{2}{\pi k\Delta_{r_n,r}}} + \frac{2}{(kd)^2}.
\end{aligned} \tag{30}$$

Therefore, for any reconstruction point r in the source plane, $\gamma(r)$ approaches the zero vector in the limit of high frequencies. This, together with equation (27), leads to

$$\lim_{k\to\infty} \alpha(r) = 0. \tag{31}$$

This proves that, although the ansatz of SONAH clearly contains frequency domain beamforming as a possible outcome, it is neither the limit of high wavenumbers k nor, as a similar computation proves, the limit of large distances d to the source plane. The reconstructed pressures approach zero in the limit of high frequencies.

2.2 HELS

The starting point for the HELS method (see [10]) is the Helmholtz equation in spherical coordinates. Again, let $p : \mathbb{R}^3 \to \overline{\mathbb{C}}$ be the complex amplitude of a time-harmonic sound pressure field of angular frequency ω and speed of propagation c. By definition, p satisfies the Helmholtz equation

$$\frac{\partial^2 p}{\partial x^2} + \frac{\partial^2 p}{\partial y^2} + \frac{\partial^2 p}{\partial z^2} + k^2 p = 0, \quad k = \frac{\omega}{c}. \tag{32}$$

Let $\hat{p} : [0, \infty] \times [0, \pi] \times [0, 2\pi] \to \overline{\mathbb{C}}$ be p's representation in spherical coordinates (r, θ, ϕ). Consequently, $\hat{p}$ satisfies

$$\frac{1}{r^2}\frac{\partial}{\partial r}\left(r^2 \frac{\partial \hat{p}}{\partial r}\right) + \frac{1}{r^2 \sin\theta}\frac{\partial}{\partial \theta}\left(\sin\theta \frac{\partial \hat{p}}{\partial \theta}\right) + \frac{1}{r^2 \sin^2\theta}\frac{\partial^2 \hat{p}}{\partial \phi^2} + k^2 \hat{p} = 0. \tag{33}$$

Solutions to this equation can be found analytically by assuming that $\hat{p}$ is separable, i.e. there exist functions $R : [0, \infty] \to \overline{\mathbb{C}}$, $\Theta : [0, \pi] \to \overline{\mathbb{C}}$, $\Phi : [0, 2\pi] \to \overline{\mathbb{C}}$ such that

$$\hat{p}(r, \theta, \phi) = R(r) \cdot \Theta(\theta) \cdot \Phi(\phi). \tag{34}$$

In this case, equation (33) leads to

$$R(r) = A \cdot h_l^{(1)}(kr) + B \cdot h_l^{(2)}(kr) \tag{35}$$

for some constants $A, B \in \mathbb{C}$ and $l \in \mathbb{N}_0$, and $h_l^{(1)}$, $h_l^{(2)}$ denote the spherical Hankel functions of the first and second kind, respectively. Moreover, we have

$$\Theta(\theta) \cdot \Phi(\phi) = Y_l^m(\theta, \phi), \tag{36}$$

where $m \in \{-l, \ldots, l\}$, and Y_l^m is the spherical harmonic.

Motivated by Sommerfeld's radiation condition (see [12]), one of the fundamental assumptions of the HELS method is that (in the area of interest) $\hat{p}$ is approximated by a superposition of the first $J = L(L+1) + M + 1$ outgoing separable solutions,

$$\begin{aligned}\hat{p}(r, \theta, \phi) \approx \hat{p}_{\text{app}}(r, \theta, \phi) &= \sum_{l=0}^{L-1} \sum_{m=-l}^{l} \alpha_{ln} \cdot h_l^{(2)}(kr) \cdot Y_l^m(\theta, \phi) \\ &\quad + \sum_{m=-L}^{M} \alpha_{Ln} \cdot h_L^{(2)}(kr) \cdot Y_L^m(\theta, \phi),\end{aligned} \tag{37}$$

$$\alpha_{ln} \in \mathbb{C}, \quad L \geq 1, \quad M \in \{-L, \ldots, L\}. \tag{38}$$

Based on a measurement of $\hat{p}$ at the positions (r_n, θ_n, ϕ_n), $n = 1, \ldots, N$, the HELS method determines $\hat{p}_{\text{app}}$ as follows. Initially, it decomposes the set of measurement indices into two disjoint subsets,

$$I_S \dot{\cup} I_R = \{1, \ldots, N\}, \quad \#I_S = \begin{cases} \#I_R & N \text{ even} \\ \#I_R + 1 & N \text{ odd} \end{cases}. \tag{39}$$

Then, for each number J of outgoing separable solutions under consideration, it determines the least squares solution $\hat{p}_{\text{app}}^J$ of (37) using the solving positions (r_n, θ_n, ϕ_n), $n \in I_S$ and computes its error Δ_J at the remaining positions,

$$\Delta_J = \sum_{n \in I_R} \left| \hat{p}\left(r_n, \theta_n, \phi_n\right) - \hat{p}_{\text{app}}^J \left(r_n, \theta_n, \phi_n\right) \right|^2. \tag{40}$$

Finally, $\hat{p}_{\text{app}}$ is chosen to be the least squares solution with the smallest error,

$$\hat{p}_{\text{app}} = \hat{p}_{\text{app}}^{J_{\min}}, \quad \Delta_{J_{\min}} = \min_J \Delta_J. \tag{41}$$

A more elaborate variant of the HELS method utilizing the modified Tikhonov regularization (see [13]) together with the generalized cross-validation (see [14]) is discussed in [10].

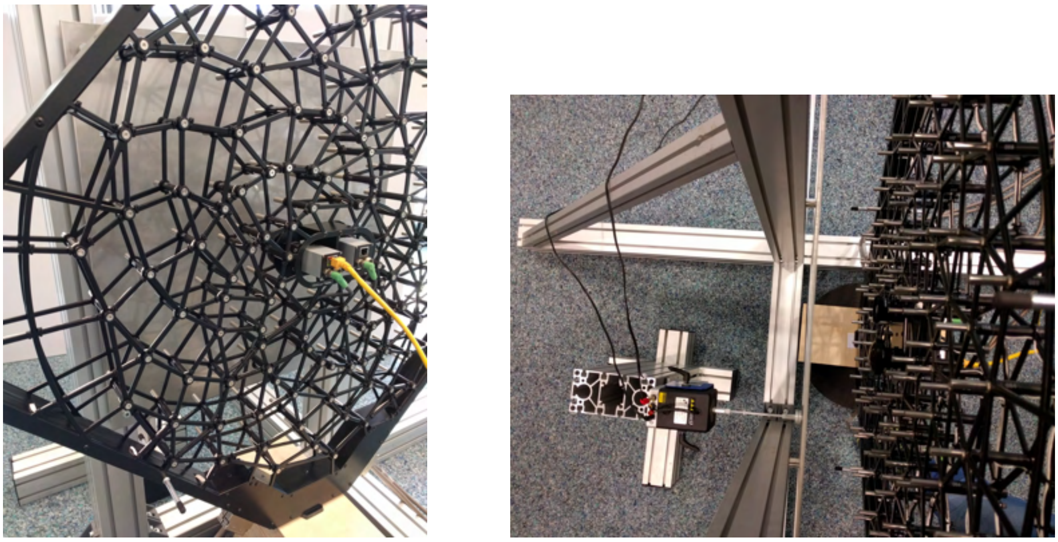

Figure 2. Experimental setup for acoustical holography, front view (left) and top view (right)

3. EXPERIMENTAL SETUP

Two (series of) measurements have been performed on a vibrating plate. A first series of laser-vibrometer measurements provided the necessary information to perform a modal analysis of the plate. A second series of acoustic measurements allowed to compare this analysis against the results of the acoustical holography methods discussed section 2 (see section 4 for results). The following items were used during both measurement sessions:

- PCB SmartShaker with Integrated Power Amplifier, Model K2007E01
- Stainless steel plate of dimension 600 mm × 600 mm × 4 mm fixed at each corner with bolts using a torque of 10 Nm
- RME Fireface UCX external sound card controlled from the measurement PC, the excitation signal was white noise generated by Audacity

The system and settings used for the modal analysis were:

- Polytec PSV-500 Scanning Vibrometer Full-Field Vibration Measurement System acquiring particle velocity data at 33×33 points covering 51 cm × 51 cm of the central part of the steel plate, the bolts were outside the scanning area
- Acquisition was done at 5 kHz, using 1600 FFT lines and 66 $\%$ overlap
- Polytec Scanning Presentation software was used for ODS analysis and the modal curve fitting done in WaveImage

The items that were used during the acoustic measurement and the later analysis include:

- Acoustic Camera Fibonacci 120 multi-purpose phased array, its microphones were placed centrally at 10 cm distance to the steel plate
- Acoustic Camera mcdRec 721B data acquisition system, each measurement sampled 64 s at a rate of 192 kHz
- NoiseImage recording and analysis software

Both measurement sessions took place in a quiet room at the GFaI offices in Berlin. The experimental setup for the acoustical holography measurement is presented in Figure 2.

4. RESULTS

For comparing the results of the laser vibrometer measurement and the acoustical holography methods, all plots that follow (see Figure 3-16) show the same section of the plate, i.e. the section of dimension 51 cm × 51 cm that was scanned by the laser vibrometer. Moreover, for each coefficient or vibration mode, the corresponding three plots show the magnitude of the particle velocity using the same dynamic and color scale.

To be be as close to reality as possible, the laser vibrometer measurement and the acoustical measurement were done at the same plate but on different days rebuilding the setup. This was done in a most reproducible way, but slight frequency shifts of the vibration modes were expected. However, up to the methodical differences in frequency resolution, most of the modes determined by the laser vibrometer were found acoustically at the same frequency. The only exception are the vibration modes at 363.8 Hz and 463.8 Hz (see Figure 12 and 14).

The geometric center for the HELS basis functions was set 36 cm behind the center of the plate, the number of outgoing separable solutions was ranging from $J = 4$ to $J = 81$. Especially in frequencies below 200 Hz, HELS performed quite well. However, being a true near-field method, the measurement distance of 10 cm clearly limited the performance of HELS. Moreover, a higher maximal number of outgoing separable solutions together with the modified Tikhonov regularization method mentioned in subsection 2.2 might have led to better results for higher frequencies.

Since there are no microphones in the very center of the phased array (cf. Figure 1), both acoustical holography methods show tendencies to deviate in the center of the reconstruction area (see Figure 3, 4, 6 and 8 for examples).

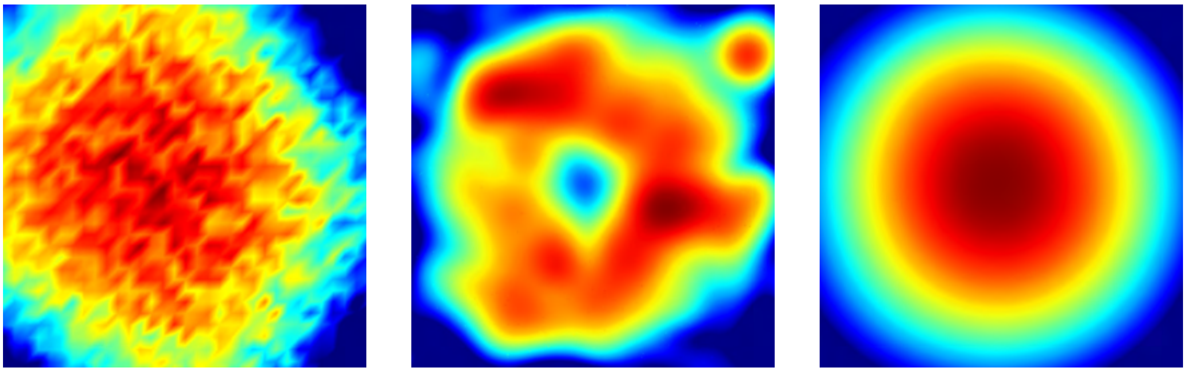

Figure 3: Magnitude of particle velocity, 15 dB dynamic, laser vibrometer at 36.3 Hz (left), SONAH (middle) and HELS (right) both at 35.2 Hz

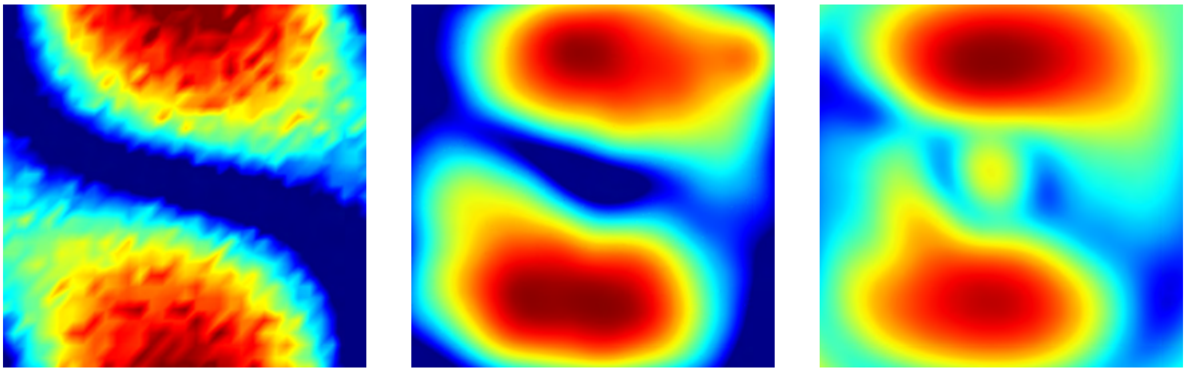

Figure 4: Magnitude of particle velocity, 17 dB dynamic, laser vibrometer at 65.0 Hz (left), SONAH (middle) and HELS (right) both at 64.5 Hz

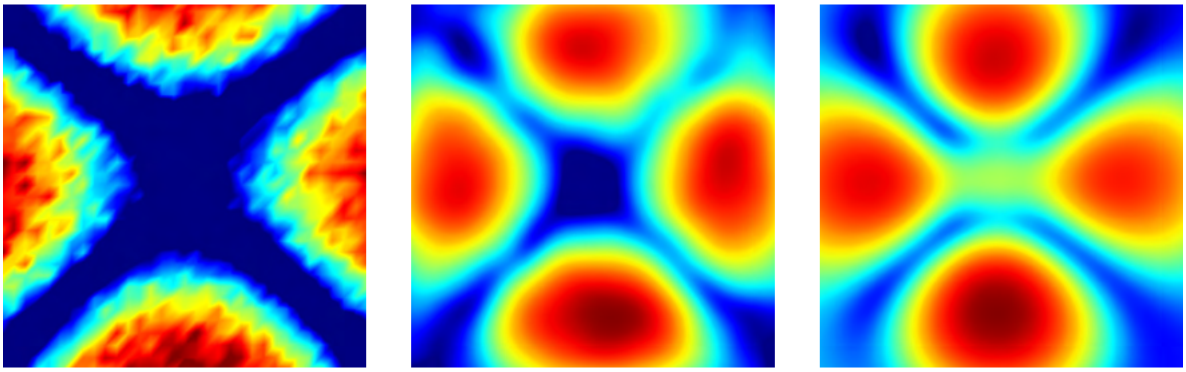

Figure 5: Magnitude of particle velocity, 17 dB dynamic, laser vibrometer at 80.0 Hz (left), SONAH (middle) and HELS (right) both at 79.1 Hz

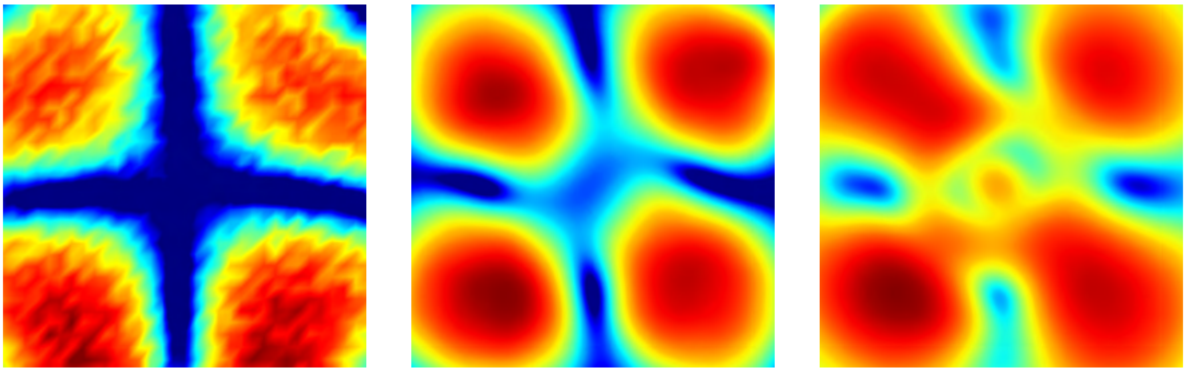

Figure 6: Magnitude of particle velocity, 19 dB dynamic, laser vibrometer at 142.5 Hz (left), SONAH (middle) and HELS (right) both at 143.6 Hz

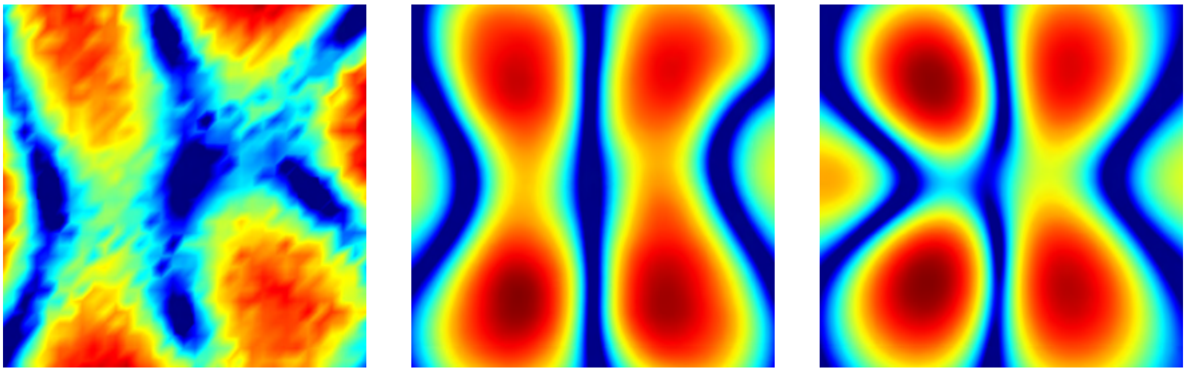

Figure 7: Magnitude of particle velocity, 20 dB dynamic, laser vibrometer at 166.3 Hz (left), SONAH (middle) and HELS (right) both at 167.0 Hz

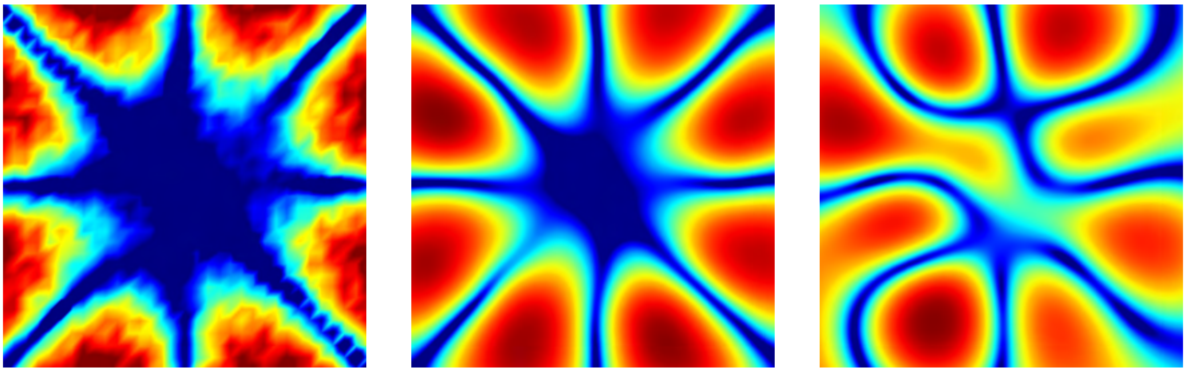

Figure 8: Magnitude of particle velocity, 24 dB dynamic, laser vibrometer at 220.0 Hz (left), SONAH (middle) and HELS (right) both at 219.7 Hz

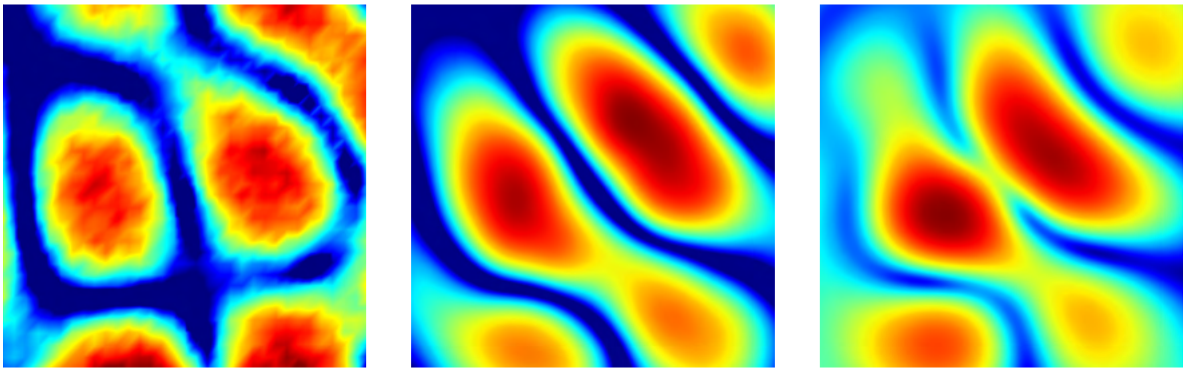

Figure 9: Magnitude of particle velocity, 20 dB dynamic, laser vibrometer at 258.8 Hz (left), SONAH (middle) and HELS (right) both at 257.8 Hz

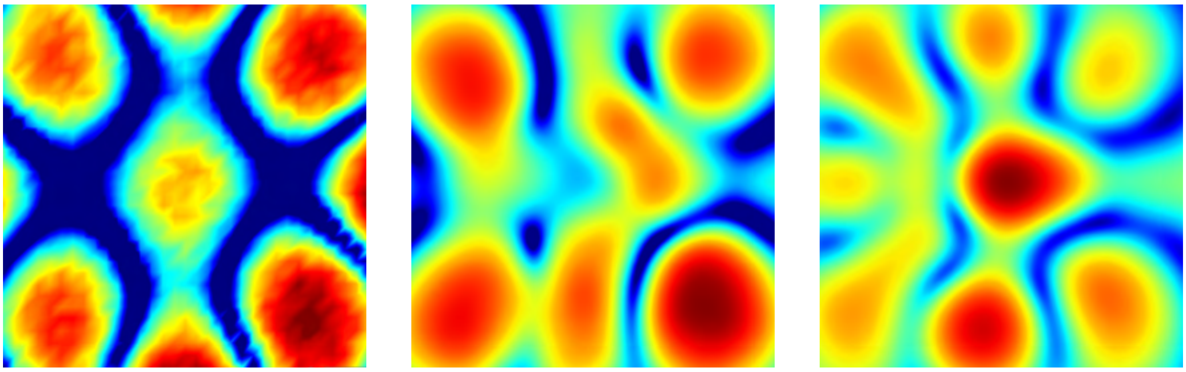

Figure 10: Magnitude of particle velocity, 20 dB dynamic, laser vibrometer at 305.0 Hz (left), SONAH (middle) and HELS (right) both at 304.7 Hz

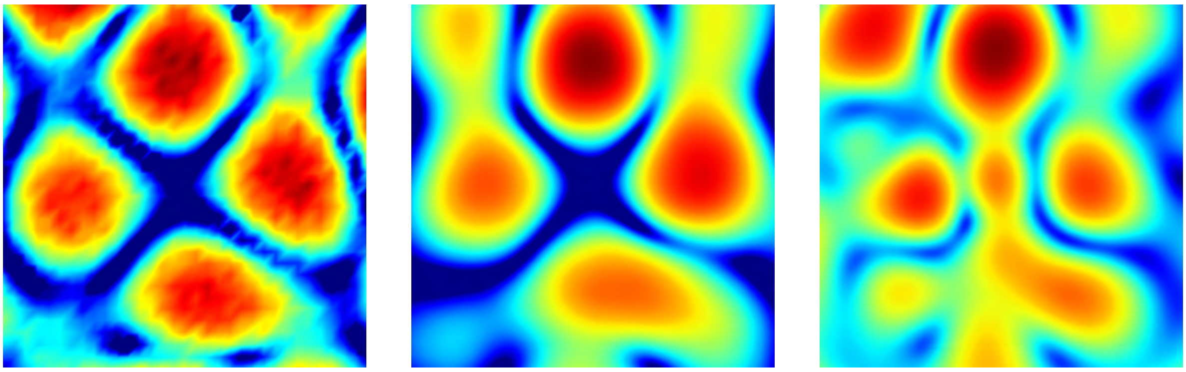

Figure 11: Magnitude of particle velocity, 22 dB dynamic, laser vibrometer at 347.5 Hz (left), SONAH (middle) and HELS (right) both at 345.7 Hz

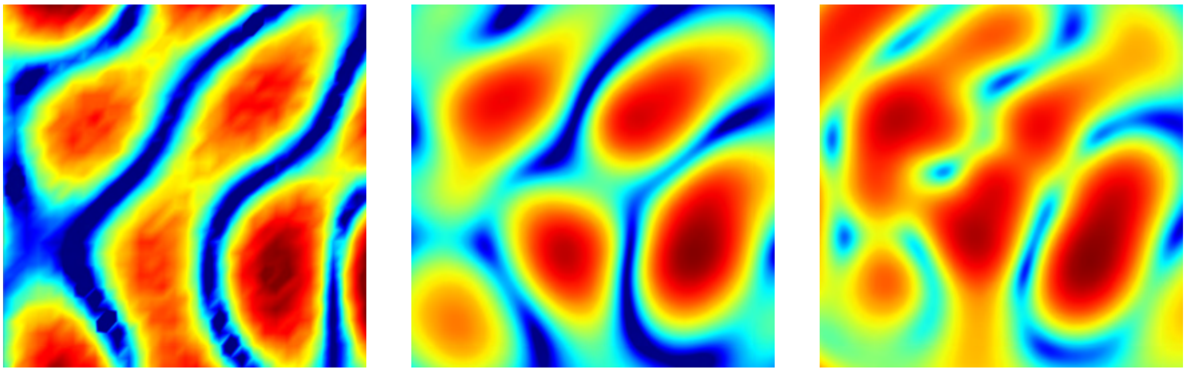

Figure 12: Magnitude of particle velocity, 22 dB dynamic, laser vibrometer at 363.8 Hz (left), SONAH (middle) and HELS (right) both at 375.0 Hz

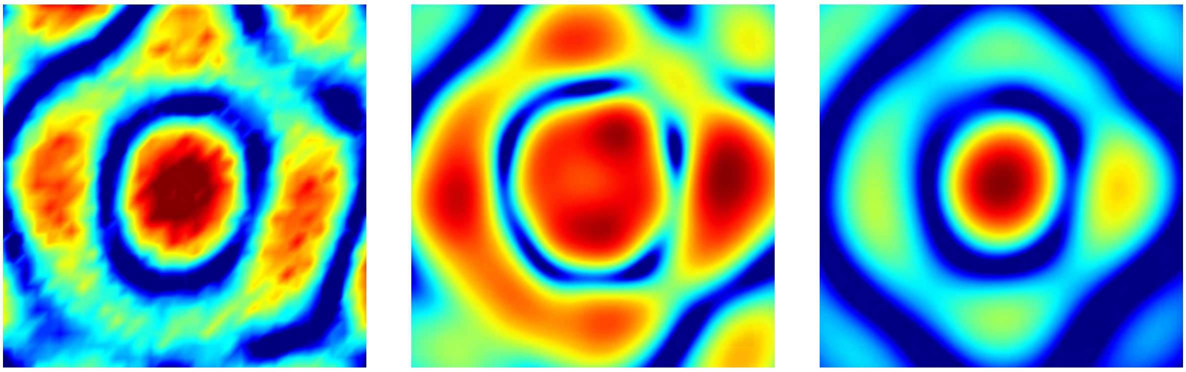

Figure 13: Magnitude of particle velocity, 18 dB dynamic, laser vibrometer at 400.0 Hz (left), SONAH (middle) and HELS (right) both at 401.4 Hz

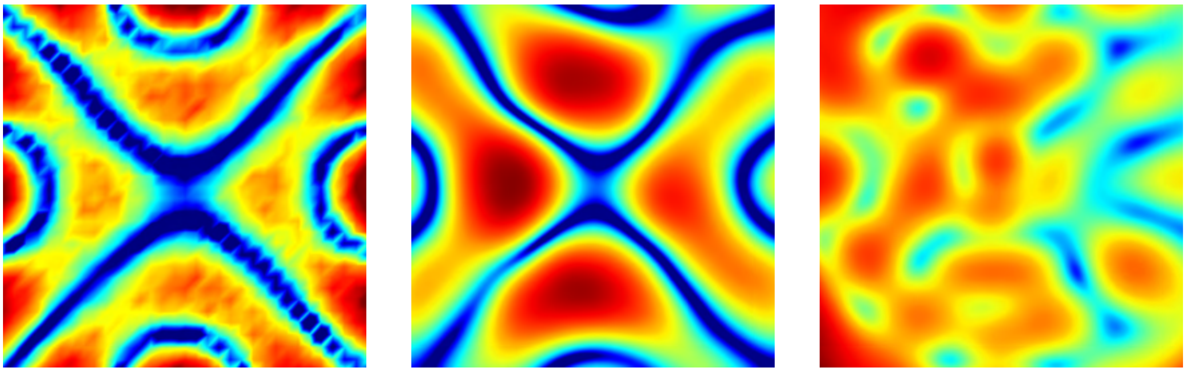

Figure 14: Magnitude of particle velocity, 24 dB dynamic, laser vibrometer at 463.8 Hz (left), SONAH (middle) and HELS (right) both at 460.0 Hz

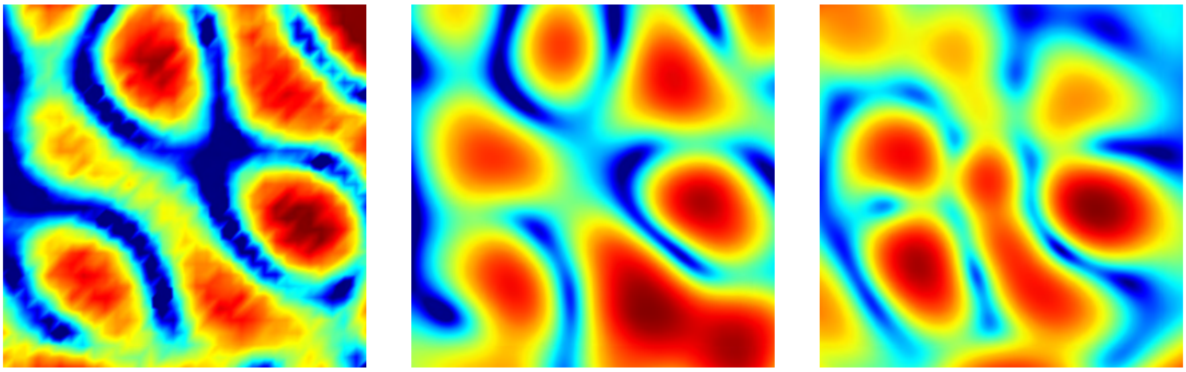

Figure 15: Magnitude of particle velocity, 20 dB dynamic, laser vibrometer at 490.0 Hz (left), SONAH (middle) and HELS (right) both at 486.3 Hz

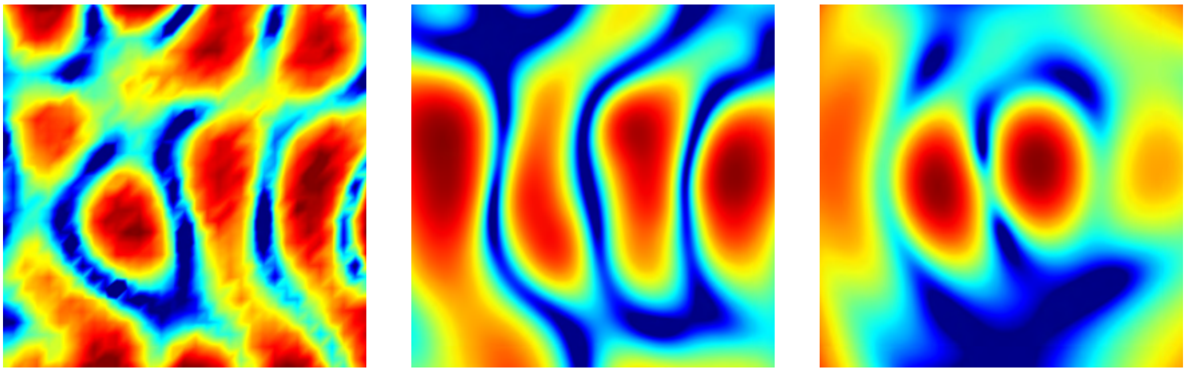

Figure 16: Magnitude of particle velocity, 20 dB dynamic, laser vibrometer at 633.8 Hz (left), SONAH (middle) and HELS (right) both at 632.8 Hz

REFERENCES

[1] D.H. Johnson and D.E. Dudgeon. *Array signal processing: concepts and techniques*. Prentice Hall, 1993.

[2] A. Nordborg, J. Wedemann, and L. Willenbrink. Optimum array microphone configuration. In *Proceedings of the 29th International Congress and Exposition on Noise Control Engineering*. SFA, 2000.

[3] C. Schulze, E. Sarradj, and A. Zeibig. Characteristics of microphone arrays. In *Proceedings of the 33rd International Congress and Exposition on Noise Control Engineering*, 2004.

[4] Z. Prime and C. Doolan. A comparison of popular beamforming arrays. In *Proceedings of the 2013 Annual Conference of the Australian Acoustical Society*, 2013.

[5] E. Sarradj. A generic approach to synthesize optimal array microphone arrangements. In *Proceedings of the 6th Berlin Beamforming Conference*, 2016.

[6] E.G. Williams. *Fourier acoustics: sound radiation and nearfield acoustical holography*. Academic Press, 1999.

[7] H. Vogel. A better way to construct the sunflower head. *Mathematical Biosciences*, 44(3):179–189, 1979.

[8] J.N. Ridley. Packing efficiency in sunflower heads. *Mathematical Biosciences*, 58(1):129–139, 1982.

[9] R. Steiner and J. Hald. Near-field acoustical holography without the errors and limitations caused by the use of spatial DFT. *International Journal of Acoustics and Vibration*, 6(2):83–89, 2001.

[10] S.F. Wu. *The Helmholtz equation least squares method*. Modern Acoustics and Signal Processing. Springer, New York, 2015.

[11] H. Weyl. Ausbreitung elektromagnetischer Wellen über einem ebenen Leiter. *Annalen der Physik*, 365(21):481–500, 1919.

[12] A. Sommerfeld. *Partial differential equations in physics*, volume 1 of *Pure and Applied Mathematics*. Academic Press, New York, 1949.

[13] E.G. Williams. Regularization methods for near-field acoustic holography. *Journal of the Acoustical Society of America*, 110(4):1976–1988, 2001.

[14] G.H. Golub, M. Heath, and G. Wahba. Generalized cross-validation as a method for choosing a good ridge parameter. *Technometrics*, 21(2):215–223, 1979.